Article

Proton Dynamics in *N,N,N#,N#*-Tetramethylguanidinium Bis(perfluoroethylsulfonyl)imide Protic Ionic Liquid Probed by Quasielastic Neutron Scattering

Eugene Mamontov, Huimin Luo, and Sheng Dai

More About This Article

Additional resources and features associated with this article are available within the HTML version:

- Supporting Information
- Access to high resolution figures
- Links to articles and content related to this article
- Copyright permission to reproduce figures and/or text from this article

View the Full Text HTML

ACS Publications
High quality. High impact.

Proton Dynamics in *N,N,N′,N′*-Tetramethylguanidinium Bis(perfluoroethylsulfonyl)imide Protic Ionic Liquid Probed by Quasielastic Neutron Scattering

Eugene Mamontov,*,† Huimin Luo,‡ and Sheng Dai§

*Neutron Scattering Science Division, Oak Ridge National Laboratory, Oak Ridge, Tennessee 37831-6473;
Nuclear Science and Technology Division, Oak Ridge National Laboratory, Oak Ridge, Tennessee 37831-6181;
and Chemical Sciences Division, Oak Ridge National Laboratory, Oak Ridge, Tennessee 37831-6201*

Using quasielastic neutron scattering, we have investigated diffusion dynamics of protons in the protic ionic liquid, *N,N,N′,N′*-tetramethylguanidinium bis(perfluoroethylsulfonyl)imide, a promising new compound for application as an electrolyte in proton-conducting fuel cells. A temperature range of 30−360 K has been studied. The melting temperature of *N,N,N′,N′*-tetramethylguanidinium bis(perfluoroethylsulfonyl)imide is about 290 K. We have found four distinct dynamic processes. First, the methyl group rotations exhibit broadly distributed dynamics which, on the nanosecond time scale, become visible above approximately 100 K. Second, there is a localized process with a characteristic confinement radius of about 1.6 Å, which likely involves protons of the −NH₂ groups. These two processes take place in both solid and liquid phases, even though the methyl group rotations in the liquid phase are likely too fast to be detected in our experiment. Above the melting temperature, there are two new diffusion processes contributing to the dynamics of the liquid phase. Both of them appear to be of translational character. However, only the slower process represents unrestricted translation diffusion. The faster process is better described as spatially restricted translational diffusion with a characteristic confinement radius of about 8 Å. It is likely that the long-range proton transfer in *N,N,N′,N′*-tetramethylguanidinium bis(perfluoroethylsulfonyl)imide is associated primarily with the unrestricted translational diffusion process, which is characterized by a diffusion coefficient varying from 0.4×10^{-10} to 1.4×10^{-10} m²/s in the temperature range of 320−360 K.

Introduction

Protic ionic liquids (PILs) have great potential for proton-conducting fuel cell electrolytes.[1−8] These room temperature liquids exhibit many useful features, such as extremely low vapor pressure, very high conductivity, and, importantly, a large gap between the melting and decomposition temperatures. We have recently synthesized some novel PILs based on neutralization of strong organic bases (Bs) with superacids (HAs):[9]

$$HA + B = A^- + BH^+ \tag{1}$$

Among them, *N,N,N′,N′*-tetramethylguanidinium bis(perfluoroethylsulfonyl)imide ([H₂NC(dma)₂][BETI]) is an example of room-temperature PILs, which are prepared via such a strategy. The structure of [H₂NC(dma)₂][BETI] is presented in Figure 1. The pK_a value of this compound is 23.3 in acetonitrile solution, giving rise to a ΔpK_a [=pK_a(BH⁺)-pK_a(HA)] value of >30 for the neutralization reaction (eq 1).[10] This large ΔpK_a value prevents the reverse proton transfer and thereby significantly enhances its high-temperature stability. The diffusion dynamics of protons in this complex liquid are intimately tied to its performance as electrolyte, and, thus, warrant detailed investigation.[11−13]

Quasielastic neutron scattering (QENS) is a technique of choice for studying the details of diffusion dynamics of hydrogen
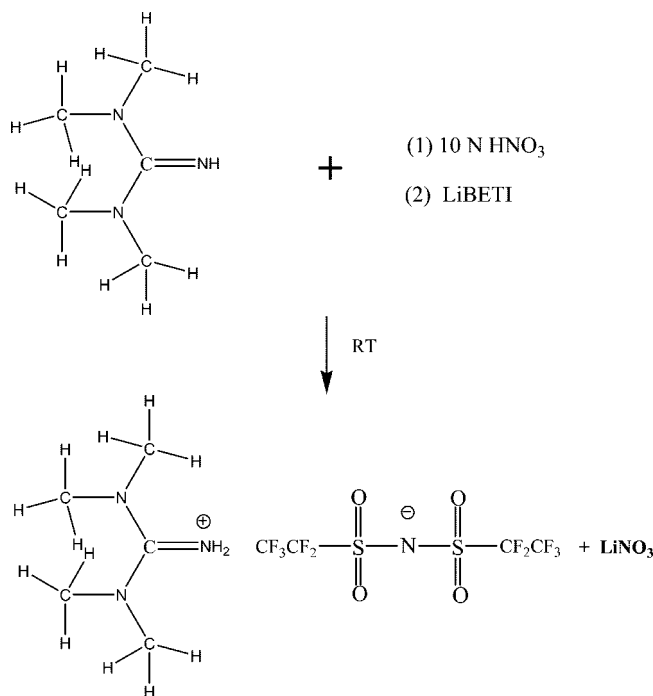

Figure 1. Structure of [H₂NC(dma)₂][BETI].

on the molecular level because of (1) the large incoherent scattering cross section of hydrogen compared to other elements and (2) capability of probing spatial characteristics of diffusion processes through dependence of the scattering signal on the momentum transfer, *Q*. The latter is a clear advantage of QENS

* To whom correspondence should be addressed. E-mail: mamontove@ornl.gov. Tel: (865) 574-5109. Fax: (865) 574-6080.
† Neutron Scattering Science Division.
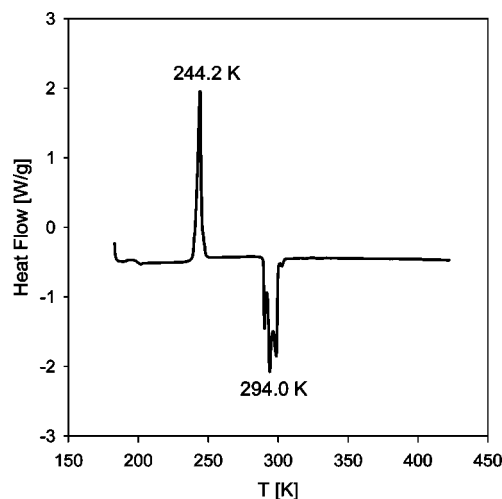‡ Nuclear Science and Technology Division.
§ Chemical Sciences Division.

Figure 2. Differential scanning calorimetry measurement of [H$_2$NC(dma)$_2$][BETI] taken on warming up at 2 K/min.

compared to, for example, NMR, and is especially beneficial for studying proton motions in complex media such as ionic liquids.[14−17] In this study, we have exploited the Q-dependence of the scattering signal to identify several dynamic processes involving diffusion motions of hydrogen atoms in [H$_2$NC-(dma)$_2$][BETI]. We have benefited from the capabilities of the new backscattering spectrometer (BASIS) at the Spallation Neutron Source (SNS), Oak Ridge National Laboratory (ORNL), which combines high counting rates, an excellent energy resolution, and a substantial dynamic range.

Experiment

Synthesis and Characterization. The [H$_2$NC(dma)$_2$][BETI] ionic liquid was synthesized in high yield in one pot via two reactions. The one-pot synthesis we developed involves the metathesis reaction of an ammonium salt [H$_2$NC(dma)$_2$][NO$_3$], prepared by the reaction of *N,N,N′,N′*-tetramethylguanidine with a common acid (e.g., HNO$_3$) and subsequently with lithium bis(perfluoroethylsulfonyl)imide (LiBETI) in an aqueous solution.[9] The resulting hydrophobic [H$_2$NC(dma)$_2$][BETI] ionic liquid phase separates from the aqueous phase. Figure 1 outlines the basic protocol for synthesis of our protic ionic liquid. The resulting [H$_2$NC(dma)$_2$][BETI] ionic liquid was characterized by NMR, and its thermal properties were investigated by thermal gravimetric analysis (TGA) and differential scanning calorimetry (DSC). The water content of [H$_2$NC(dma)$_2$][BETI] measured using a Metrohm 652 KF-coulometer was 1200 ppm. ^{1}H and ^{13}C NMR spectra were obtained in CDCl$_3$ at room temperature with a Bruker MSL-400 NMR spectrometer operating at 400.13 MHz for proton and 100.61 MHz for carbon. Proton and carbon chemical shifts are reported relative to tetramethylsilane (TMS). ^{1}H NMR data: δ, 6.02 (broad peak, 2H) and 2.99 (s, 12H). ^{13}C NMR: δ, 161.13 (C=NH$_2$), 115.66 (CF$_3$, qt, J_{C-F} = 287.4 Hz, J_{C-C-F} = 33.1 Hz), 111.68 (CF$_2$, qt, J_{C-F} = 293.9 Hz, J_{C-C-F} = 38.6 Hz), and 38.86 (CH$_3$). Thermogravimetric analysis curve was measured in nitrogen (gas flow 80/60) at a scan rate of 10 K/min with TA instrument TGA 2950. The TGA measurement shows the onset of weight loss at 317 °C, thus indicating excellent thermal stability. Differential scanning calorimetry curve was performed with a TA instruments DSC Q100. Scanning sequence involves freezing the IL sample to −90 °C (183K), maintaining this temperature for 20 min, and then heating the sample to 150 °C (423 K) at 2 K/min. The DSC plot shown in Figure 2 has a heat absorption peak at about 294

K, which may correspond to the melting point of the ionic liquid. It should be noted that [H$_2$NC(dma)$_2$][BETI] is a liquid at ambient temperature. The DSC plot also shows an exothermal peak at about 244 K, which is likely associated with crystallization of the amorphous phase above T_g on warming up. We have verified that the "multistep" appearance of the melting transition disappears if the measurements are performed at 10 K/min, which is the standard operation mode of the DSC Q100 instrument. However, we present the DSC data collected at 2 K/min in order to make a better comparison with the thermal conditions encountered in the course of the neutron measurements of the elastic scattering intensities that were performed at 2 K/min heating rate as we will explain below.

Neutron Measurements. The QENS experiment was performed on the new backscattering spectrometer, BASIS, at the SNS, ORNL. The BASIS is an inverted geometry time-of-flight near-backscattering (with the analyzers Bragg angle at about 88°) spectrometer that utilizes reflection by Si(111) crystals to select the final energy of 2082 μeV (6.267 Å) for neutrons scattered by a sample. The neutron beam incident on the sample is polychromatic, with the bandwidth defined by a set of neutron choppers.[18,19] In this study, we operated the choppers at 60 Hz and selected a dynamic range from −100 to +100 μeV (which was free of spurious scattering) for the data analysis. The energy resolution of the spectrometer, averaged over all scattering momentum transfers, was 3.4 μeV (full width at half-maximum, fwhm).

In order to minimize the effects due to multiple scattering of neutrons in the sample, the sample was loaded in a 0.1 mm thick annular cylindrical aluminum container. The sample was then sealed with an indium O-ring and mounted onto a closed-cycled refrigerator. The temperature of the sample was controlled within ±0.5 K. The data were collected at temperature set points and in the course of a temperature ramp, as we will explain below. The set of data collected at 7 K was used as the resolution function.

The data were converted from the time-of-flight to the energy transfer spectra at selected Q values using standard BASIS data reduction software.[20] For the data analysis, the data at a particular Q value were fit using the following expression:

$$I(E) = [x\delta(E) + (1 - x)S(E) + B(E)] \otimes R(E) \quad (2)$$

Here δ(E) is a delta function centered at zero energy transfer, x represents the fraction of the elastic scattering (which might be either set to zero or allowed to vary), $B(E)$ is the background term, $R(E)$ is the resolution function, and $S(E)$ is the model scattering function. In this form, the term x represents just the elastic scattering originating from the species (hydrogenous or not) that are truly immobile on the time scale of the experiment. In addition to this term, there may be some elastic scattering that is a part of the model scattering function, $S(E)$; for instance, if this model scattering function describes a spatially confined diffusion process. In our analysis, we employed various functional forms of $S(E)$, as we will discuss below. We used the background term in the form of $B(E) = B_1 + B_2(E + E_0)^{-1}$, where the elastic energy E_0 = 2082 μeV. This functional form accounts for both processes that are too fast on the time scale of the experiment (that is, faster than a few picoseconds) and a possible constant (but sample- and temperature-dependent) background in the time-of-flight. Upon conversion from the time-of-flight to energy transfer, E, such a background would yield the component proportional to $(E + E_0)^{-3/2}$. Because of the application of inelastic scattering kinematic factor, k_i/k_f =

$((E + E_0)/E_0)^{1/2}$, in the course of data reduction, this contribution becomes proportional to $(E + E_0)^{-1}$. Since the precise evaluation and subtraction of the time-of-flight background in our experiment was difficult, it was more practical to use the background term for the data fits.

Results and Discussion

Temperature Dependence of Elastic and Quasielastic Signals. In order to evaluate qualitatively the temperature dependence of the QENS intensity and identify the temperature regions that may warrant further exploration, we began our scattering experiment with an "intensity scan", recording the data every 10 min while ramping up the temperature from 30 to 350 K at a rate of 2 K/min. A similar technique, usually called "elastic intensity scan", is often employed at the reactor-based backscattering spectrometers. In this case, only the elastic intensity, measured at zero energy transfer with the Doppler-driven monochromator at rest, is monitored as function of temperature. The time efficiency and high throughput of elastic intensity scans is achieved at the expense of losing information about the dynamics on various time scales, which is only available from full dynamic measurement. In other words, the quick data collection is achieved by means of sampling only one value of the energy transfer. On a time-of-flight backscattering spectrometer such as the BASIS, all energies transfers are sampled simultaneously due to the polychromatic incident beam, and selecting only the elastic line for the data analysis does not provide a time advantage. However, the signal intensity measured at the spectrometer needs to be very high in order to successfully analyze not only the (typically) much stronger elastic peak but also the (typically) much weaker quasielastic wings in sets of data collected in a short time (that is, per one temperature point of the intensity scan).

In our experiment, we attempted, for the first time, to determine whether the high intensity of the BASIS is sufficient to extract full dynamic information (as opposed to merely the elastic intensity) while recording the data over short time intervals of several minutes when ramping the temperature at a rate of 1–2 K/min. As we will discuss below, for a strongly scattering hydrogenous sample such as [H$_2$NC(dma)$_2$][BETI], analyzing full dynamic information collected in several minutes per one point of an "intensity scan" is currently possible if the data can be averaged over all Q values. One can fully expect that even full dynamic analysis of Q-dependent data obtained using "intensity scans" will be possible once the SNS reaches its full power of 1.4 MW. The data reported in this work were collected when the SNS power was about 400 kW.

Figure 3 shows the results of intensity scans binned to four different average values of Q, while Figure 4 shows the results of integration of the data in Figure 3 over the -3.4μeV $< E <$ 3.4 μeV range of the energy transfer, corresponding to the spectrometer resolution function. Results qualitatively similar to those presented in Figure 4 could be obtained using an elastic intensity scan on a reactor-based backscattering spectrometer with a Doppler-driven monochromator at rest.

As the temperature is increased above the baseline temperature of a scan, the scattering intensity at the elastic line typically decreases due to Debye–Waller thermal factors. This is because a certain fraction of the elastic scattering intensity, which increases with temperature, becomes redistributed to the inelastic (vibrational) channels. If there are no species in the sample that become mobile on the time scale of the spectrometer resolution within the temperature range scanned, then the elastic intensity merely monotonically decreases as the temperature is increased.

In the presence of species that become mobile above certain temperature, either due to a freezing–melting transition, or because their diffusion dynamics become faster than the spectrometer resolution window (for the BASIS, about a nanosecond), there is a faster, significant reduction in the elastic intensity in addition to the normal Debye–Waller behavior. This is because, in addition to the redistribution of the elastic intensity to the vibrational channels, there is a very significant redistribution to the quasielastic scattering channels.

In systems which are characterized by a distribution of diffusion dynamics, the intensity of the QENS wings gradually grows above the temperature at which the dynamics of the fastest species enters the spectrometer resolution window. At the same time, the intensity of the elastic signal gradually decreases, in both QENS data such as those shown in Figure 3 and elastic data such as those shown in Figure 4. This is because a progressively higher fraction of the diffusion dynamics distribution enters the spectrometer resolution window, and the QENS signal generally becomes broader, contributing less to the scattering near the elastic line. Typically, at even higher temperatures, the elastic scattering intensity does not decrease rapidly with temperature any more, because the fraction of species mobile on the time scale of the spectrometer resolution eventually becomes saturated, and the QENS signal becomes too broad compared to the resolution function to affect the elastic intensity. On the other hand, a freezing–melting transition typically manifests itself in an abrupt drop in the elastic intensity and concurrent abrupt development of the QENS wings.

In the data presented in Figures 3 and 4, there is no evidence of diffusion mobility up to about 100 K. Below this temperature, there is only a gradual reduction in intensity as the temperature is raised due to Debye–Waller thermal factors. Above about 100 K, at all Q values except the lowest $Q = 0.4$ Å^{-1}, the elastic intensity decreases relatively fast until about 210–230 K, before reaching a plateau. At about 290 K, there is a dramatic decrease in the spectra collected at all Q values due to a freezing-melting transition. The lack of features in the lowest-Q elastic spectrum below 290 K (except the expected Debye–Waller decrease with temperature) clearly indicates the localized character of diffusion dynamics of hydrogen atoms in the solid phase. We attribute the dynamics dominating the $Q = 0.8$ Å^{-1}, $Q = 1.2$ Å^{-1}, and $Q = 1.6$ Å^{-1} spectra between about 100 and 220 K to the well-known mechanism of rotations of methyl groups. The rotation dynamics of methyl groups is known to enter the nanosecond time scale above 100 K (thereby becoming visible in the neutron inelastic spectra) in many classes of materials, such as polymers[21] and proteins.[22] Furthermore, previous QENS studies of an ionic liquid 1-butyl-3-methylimidazolium hexafluorophosphate ([bmim][PF$_6$]) by Triolo et al. have attributed the more rapid intensity decrease in the elastic scans above about 100 K to the methyl group rotations.[14–16] As a universal phenomenon not specific to a particular compound that involves only the localized (rotational) motions of hydrogen atoms, the rotational dynamics of methyl groups are of the least interest to us. On the other hand, the temperature range between about 240 and 290 K warrants further investigation. This is because the higher-Q spectra in Figure 3 shows some QENS broadening in this temperature range, indicating hydrogen dynamics which are localized, but different from the methyl group rotations. The higher-Q spectra in Figure 4 bear a striking resemblance to the elastic intensity spectra previously observed for [bmim][PF$_6$] ionic liquid, where the pronounced plateau below the melting temperature was due to crystallization of the low-temperature amorphous phase above T_g.[14–16] The onset of the plateau in our
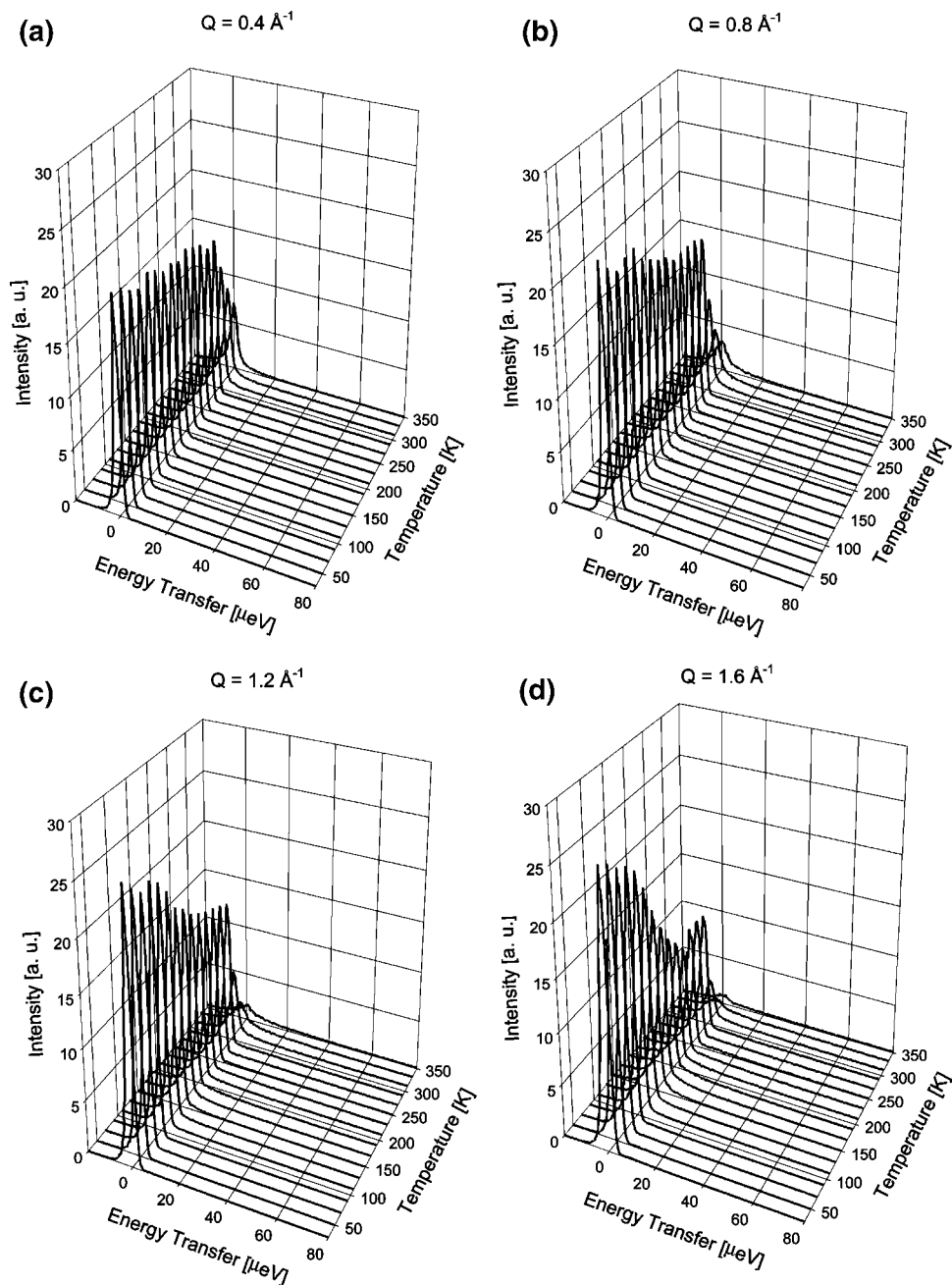
(a)   Q = 0.4 Å⁻¹

(b)   Q = 0.8 Å⁻¹

(c)   Q = 1.2 Å⁻¹

(d)   Q = 1.6 Å⁻¹

Figure 3. Scattering data collected from the [H$_2$NC(dma)$_2$][BETI] sample while the temperature was ramped up at 2 K/min at (a) $Q = 0.4$ Å^{-1}, (b) $Q = 0.8$ Å^{-1}, (c) $Q = 1.2$ Å^{-1}, (d) $Q = 1.6$ Å^{-1}.

data is also in agreement with our DSC results that show an exothermal peak due to crystallization. Importantly, both the QENS and DCS measurements were performed on warming up the low-temperature phase at the same rate of 2 K/min. Therefore, the QENS data in the temperature region of about 240−290 K were likely collected from the crystalline phase, whereas at lower temperatures the ionic liquid was in the amorphous state. Eventually, the solid phase undergoes a melting transition at about 290 K, again, in agreement with the DSC data.

Following completion of the data collection with the temperature ramp, we have selected a temperature of 260 K (approaching this point from low temperatures), in the middle of the plateau in the elastic scattering data, for data collection with higher statistics to attempt a more detailed analysis of the Q dependence of the scattering. In addition, higher statistics

data were collected for the liquid phase, at temperatures of 320, 330, 340, 350, and 360 K.

Diffusion Dynamics in the Solid Phase. As an example, the data obtained at 260 K at a selected $Q = 0.7$ Å^{-1} are presented in Figure 5 (bottom) along with the fits that will be explained below. We found that the 260 K data can be successfully fit using eq 2 with a very simple model scattering function in the form of a single Lorentzian and elastic line:

$$S(E) = \text{EISF}\delta(E) + (1 - \text{EISF})\frac{1}{\pi}\frac{\Gamma}{E^2 + \Gamma^2} \quad (3)$$

where EISF is the elastic incoherent structure factor commonly defined as the ratio of elastic to the total (elastic and quasielastic) scattering intensities. The Q-dependence of the Lorentzian half-

Proton Dynamics in [H₂NC(dma)₂][BETI]

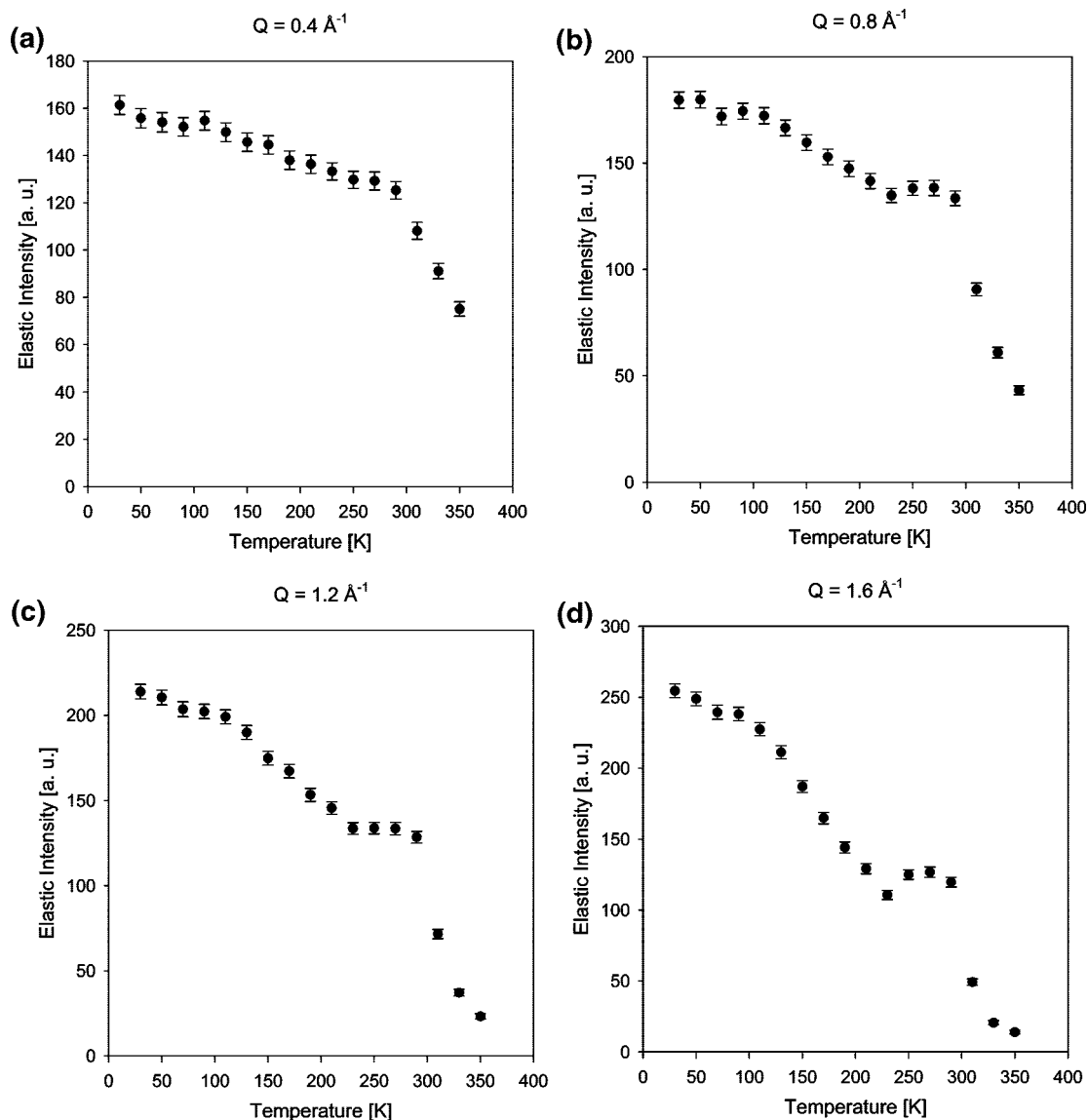*J. Phys. Chem. B, Vol. 113, No. 1, 2009* **163**

Figure 4. Elastic intensities obtained from the data shown in Figure 3 by means of integrating over the energy transfers within the elastic line, $-3.4\ \mu eV < E < 3.4\ \mu eV$: (a) $Q = 0.4\ Å^{-1}$, (b) $Q = 0.8\ Å^{-1}$, (c) $Q = 1.2\ Å^{-1}$, (d) $Q = 1.6\ Å^{-1}$.

width at half-maximum (hwhm), Γ, is shown in Figure 6a. The QENS broadening at 260 K is essentially Q-independent, which suggests that localized (as opposed to translational) motions give rise to this QENS signal, as one might expect in the solid phase. The experimentally measurable cumulative fraction of the elastic scattering in the signal, defined as $(x + (1 - x)\text{EISF})$, where x is defined in eq 2, is presented in Figure 6b. In the absence of detailed knowledge of the diffusion process specifics, but having recognized its localized character, we fit the data with a generic functional form for a confined process describing rotational diffusion jumps on a sphere of radius R_1

$$\text{EISF}(Q) = j_0^2(QR_1) \qquad (4)$$

where j_0 is the spherical Bessel function of zeroth order.[23] First, we fit the data assuming that all the species in the system are mobile (that is, $x = 0$ in eq 2), and the EISF accounts for the entire elastic signal. The resultant fit was of poor quality (short-dashed line in Figure 6b), and the value of the confining radius was $R_1 = 0.62$ Å, which is too small for a diffusing proton. We then repeated our fit while allowing the Q-independent parameter x to vary. The

resultant fit of a good quality, shown in Figure 6b with a solid line, yielded a confinement radius of $R_1 = 1.6$ Å, which is a reasonable value, and $x = 0.76$. Finally, in order to demonstrate that the localized motions probed at 260 K are not related to methyl group rotations, we attempted to fit the data in Figure 6b using

$$\text{EISF}(Q) = (1 + 2j_0(Qr\sqrt{3}))/3 \qquad (5)$$

(for 3-fold jumps on a circle of radius r),[23] still allowing the parameter x to vary. Using a known value of 1.78 Å for the proton–proton distance in methyl groups, which corresponds to $r = 1$ Å in eq 5, we obtained the best fit of rather poor quality with $x = 0.56$, shown with long-dashed line in Figure 6b. Clearly, the QENS signal at 260 K does not originate from the rotation of methyl groups, but from some other localized process instead.

The considerations above suggest that it may be the protons of the –NH₂ groups that dominate the QENS signal from the crystalline phase over the 240–290 K plateau, below the melting temperature. As evidenced by some increase of the elastic intensity in Figure 4 (especially Figure 4d), there is an increase in the rigidity of the ionic liquid upon the crystallization
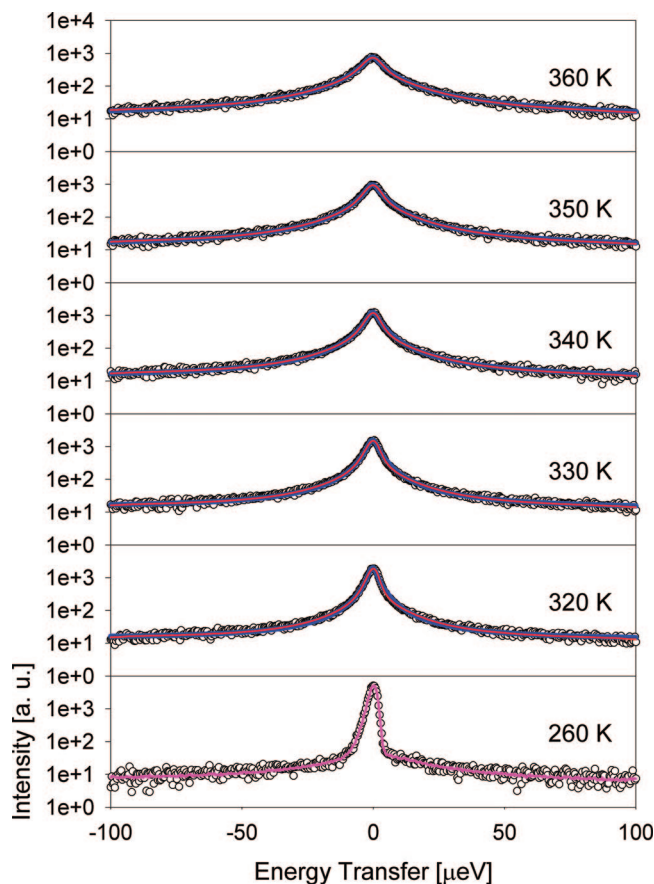
Figure 5. Symbols: QENS spectra collected at various temperatures at 0.7 Å^{-1}. Solid lines: fits obtained using eq 2 (with $x = 0$) and eq 6 (red), eq 2 (with $x = 0$) and eq 8 (blue), and, for 260 K data, eqs 2 and 3 (pink).

transition. It is possible that the dynamics of the methyl groups becomes suppressed in the crystalline phase. It should be noted that, if all the protons of the methyl groups become immobile on the time scale of the QENS measurement, thus contributing to the elastic signal only, the expected elastic scattering fraction

may be as high as $12/14 = 0.86$; we have obtained a comparable value of $x = 0.76$. Interestingly, a signature of the proton dynamics localized on the spatial scale of about 1.6 Å can be found even in the liquid phase, as we will discuss below.

Diffusion Dynamics in the Liquid Phase. Above the melting transition (the 320, 330, 340, 350, and 360 K data sets shown in Figure 5), the QENS data have the characteristic appearance of liquid spectra, with no prominent elastic line. This is because, even though both methyl group rotations and the localized proton dynamics associated with the $-NH_2$ groups persist in the liquid phase (although the former type of dynamics is likely too fast to be detected in our experiment), two new mechanisms, in which all the atoms in $[H_2NC(dma)_2][BETI]$ participate, dominate the diffusion dynamics above the melting temperature. We could not fit the data collected at the temperature set points above 290 K using a single Lorentzian, but instead had to use a two-Lorentzian model scattering function:

$$S(E) = (1 - p)\frac{1}{\pi}\frac{\Gamma_1}{E^2 + \Gamma_1^2} + p\frac{1}{\pi}\frac{\Gamma_2}{E^2 + \Gamma_2^2} \quad (6)$$

with $x = 0$ in eq 2. The Q-dependence of the Lorentzian QENS components obtained in such a way was fit with an often used expression describing a translational jump diffusion process with an exponential distribution of jump lengths:[24,25]

$$\Gamma(Q) = \frac{\hbar}{\tau}\left(1 - \frac{1}{1 + DQ^2\tau}\right) \quad (7)$$

where τ is a characteristic time between the diffusion jumps of a diffusing particle (in our case, the entire $[H_2NC(dma)_2][BETI]$ molecule). Such a diffusion process is characterized by a diffusion coefficient, $D = \langle L^2\rangle/6\tau$, where $\langle L^2\rangle$ is a mean square jump length. The fits are shown in Figure 7; the data presented in Figure 7c will be explained below.

We have also attempted to fit the liquid data with a different model scattering function:
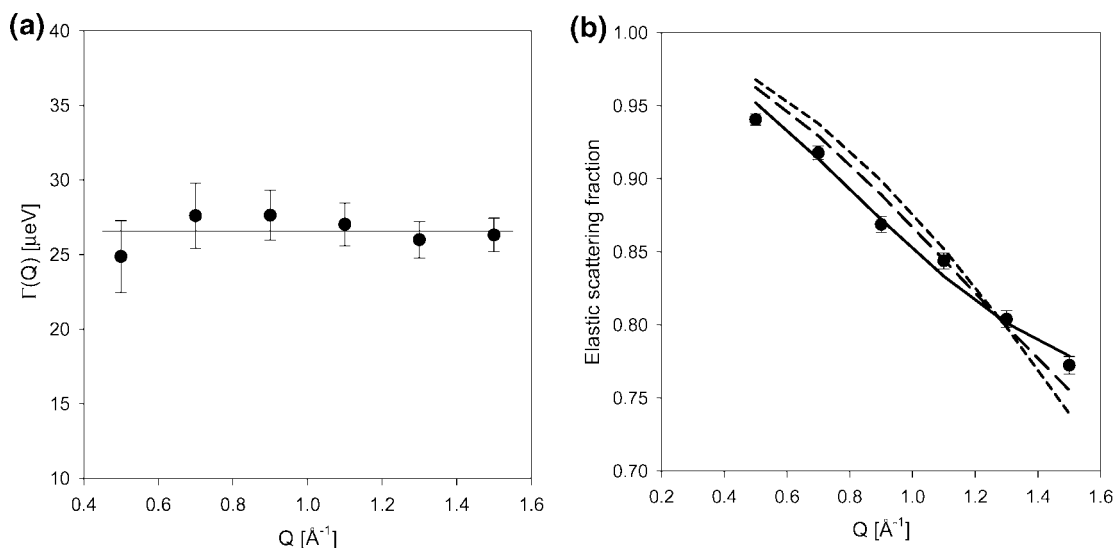

Figure 6. Parameters of the 260 K data fits obtained using eq 2 and 3. (a) Hwhm of the Lorentzian QENS broadening with a Q-independent fit. (b) Total measured elastic scattering fraction, $(x + (1 - x)EISF)$, where x is a parameter in eq 2, and its best fits obtained using EISF described by eq 4 while x was fixed to zero (short-dashed line), EISF described by eq 4 while x was allowed to vary (solid line), and EISF described by eq 5 while x was allowed to vary (long-dashed line).
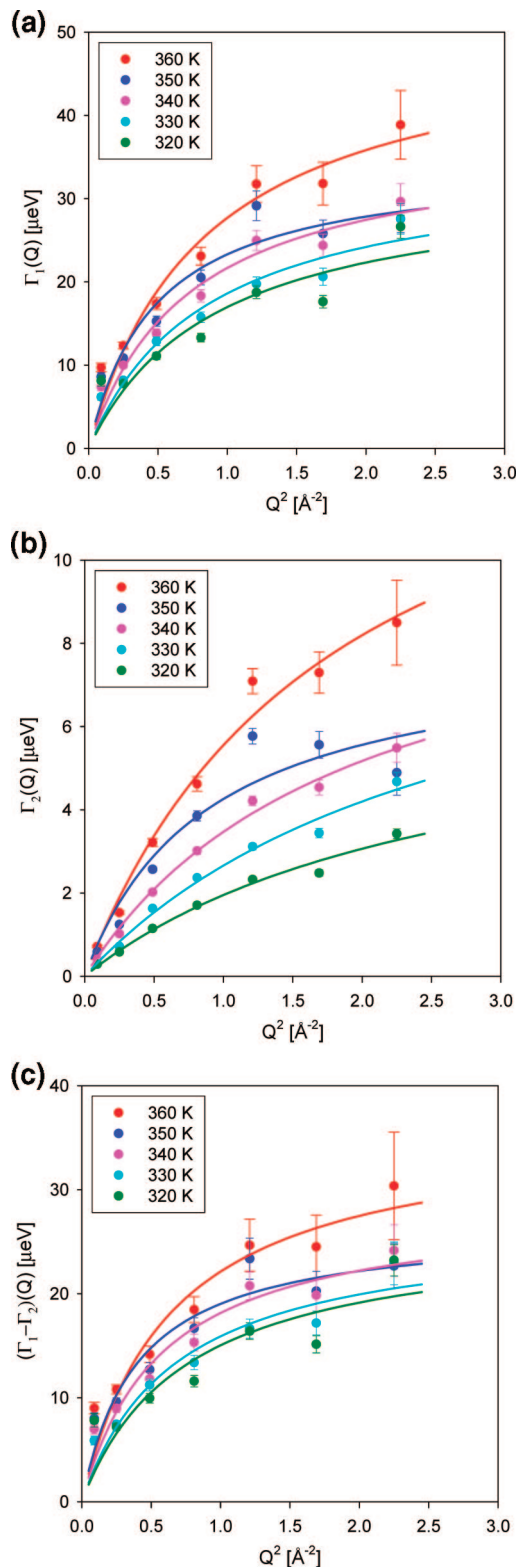
Figure 7. Symbols: temperature dependence of the hwhm of the (a) broad, Γ_1, and (b) narrow, Γ_2, Lorentzian components obtained from the data fits using eq 2 with $x = 0$ and eq 6, and (c) the narrow component subtracted from the broad component, $\Gamma_1 - \Gamma_2$. Solid lines: fits of the Q-dependence with eq 7 describing a jump diffusion model.

$$S(E) = A \int_0^\infty \exp\left[-\left(\frac{t}{\tau}\right)^\beta\right] \exp\left(i\frac{E}{\hbar}t\right) dt \qquad (8)$$

where A is a scaling constant, and $0 < \beta < 1$. This Fourier-transformed stretched exponential relaxation function is often

used to extract the average relaxation time (that one can calculate as $\langle\tau\rangle = (\tau/\beta)\Gamma(1/\beta)$, where Γ is the gamma function) for systems with a broad distribution of relaxation times. While these fits yielded a reasonable agreement with the data, comparable to that obtained using fits with two Lorentzian components (red vs blue solid lines in Figure 5), they yielded systematically worse agreement factors, as one can see in Table 1. The difference in the quality of the fits is not very pronounced at higher Q but is significant at low Q. Thus, one cannot describe the dynamics in the liquid phase as merely a superposition of various relaxation times; instead, two sets of different relaxation times (and diffusion coefficients) clearly manifest themselves, especially in the "diffusion limit" in the low-Q data. The comparison of agreement factors presented in Table 1 clearly suggest that there are two distinct diffusion processes in the liquid phase of [H₂NC(dma)₂][BETI].

This is an interesting observation that differs from previous results on [bmim][PF₆] ionic liquid.[14-16] Although two relaxation processes were considered by Triolo et al. to fit the liquid phase data from [bmim][PF₆], the faster, Debye-like β-relaxation process was characterized by very fast relaxation times (fractions of a picosecond) and localized (about 0.7 Å) spatial extent. Thus, this faster process was more similar to methyl groups or −NH₂ groups dynamics in our experiment on [H₂NC(dma)₂][BETI]. On the other hand, the slower, α-relaxation process in [bmim][PF₆] was successfully described by a single stretched exponential term, whereas we conclude that two distinct diffusion processes contribute to the dynamics of the liquid phase of [H₂NC(dma)₂][BETI].

In many simple and complex liquids, one can observe a slower translational and a faster localized (often called rotational) diffusion process. In the case of [H₂NC(dma)₂][BETI], the translational nature of both slower and faster processes is evident from the fact that the QENS broadening increases with Q. Nevertheless, the low-Q behavior of the Γ_1 (some leveling off below $Q = 0.3-0.5$ Å⁻¹, which cannot be seen in low-Q behavior of the Γ_2) suggests that the faster translational diffusion process may be spatially confined. On the basis of the discussion of confined translational diffusion within a sphere,[26,27] one can deduce a possible confinement radius of about 6.5−10 Å, calculated as $3.3/Q$, where Q is the value below which the QENS broadening remains approximately constant. We then analyzed the Q-dependence of the parameter p in eq 6, which is a spectral weight of the narrow Lorentzian, as follows.

Assuming that the faster and slower translational motions of the [H₂NC(dma)₂][BETI] molecules can be treated as independent in time and space, for each Q one can write the intermediate scattering function in the time space as a simple product, $F(t) = T_1(t)T_2(t)$, and the scattering function in the energy space as a convolution, $S(E) = T_1(E) \otimes T_2(E)$, where T_1 and T_2 represent the faster and slower translational diffusion components, respectively. Even though the exact solution of the confined diffusion equation includes an infinite series of Lorentzians,[26] one can approximate with a good precision[27] the exact functional form for the spatially constrained faster translational diffusion process by

$$T_1(t) = p + (1 - p) \exp\left[-\frac{t}{\tau_1}\right] \qquad (9)$$

where τ_1 is a Q-dependent relaxation time. The parameter p describes the Q-dependent fraction of "elastic" scattering for the constrained translational diffusion process, and may coincide with the elastic incoherent structure factor in the case when all

TABLE 1: Agreement Factor, $\chi^2 = \Sigma(I_{experiment} - I_{model})^2/(N_{observations} - N_{parameters})$, Obtained Using a Two-Lorentzian (Eq 2) with $x = 0$ and Eq 6, Denoted 2L) and a Fourier-Transformed Stretched Exponential (Eq 2) with $x = 0$ and Eq 8, Denoted SE) Model Scattering Function

	320 K		330 K		340 K		350 K		360 K	
Q (Å^{-1})	2L	SE	2L	SE	2L	SE	2L	SE	2L	SE
0.3	1.207	5.676	1.187	4.389	1.167	3.566	1.100	2.754	1.099	2.344
0.5	1.339	4.612	1.352	3.440	1.305	2.680	1.144	1.993	1.357	2.061
0.7	1.407	2.753	1.310	1.962	1.416	1.602	1.227	1.418	1.315	1.414
0.9	1.348	1.913	1.278	1.525	1.264	1.367	1.247	1.288	1.212	1.262
1.1	1.397	1.892	1.287	1.436	1.295	1.372	1.118	1.248	1.353	1.470
1.3	1.308	1.552	1.221	1.343	1.190	1.272	1.070	1.101	1.155	1.210
1.5	1.142	1.363	1.169	1.280	1.055	1.161	1.048	1.176	1.122	1.214

the species in the system are mobile and participate in the constrained diffusion process under consideration. Assuming that unrestricted translational diffusion involves molecules as a whole, the slower, not spatially constrained diffusion process is described by a simple Lorentzian:

$$T_2(t) = \exp\left[-\frac{t}{\tau_2}\right] \quad (10)$$

where τ_2 is a Q-dependent relaxation time. The convolution in the energy space is facilitated by the fact that the intermediate scattering functions that we use consist of only time-independent and exponential terms, yielding

$$T(t) = (1 - p) \exp\left[-t\left(\frac{1}{\tau_1} + \frac{1}{\tau_2}\right)\right] + p \exp\left[-\frac{t}{\tau_2}\right] \quad (11)$$

$$S(E) = (1 - p)\frac{1}{\pi} \frac{((\hbar/\tau_1) + (\hbar/\tau_2))}{E^2 + ((\hbar/\tau_1) + (\hbar/\tau_2))^2} + p\frac{1}{\pi} \frac{(\hbar/\tau_2)}{E^2 + (\hbar/\tau_2)^2} \quad (12)$$

As one can see, the parameter p in eq 12 corresponds to the parameter p in eq 6 and simply describes the spatial characteristics of the constrained diffusion process (see eq 9).

Figure 8 shows the Q-dependence of the parameter p, which we first fit using the expression

$$p(Q) = c_1 + (1 - c_1)\left(\frac{3j_1(Qa_1)}{Qa_1}\right)^2 \quad (13)$$

where j_1 is the spherical Bessel function of the first order. The parameter c_1 describes the "immobile" fraction, whereas the term in the second parentheses is the EISF for the confined translational diffusion within a sphere of radius a_1.[26,27] The parameters obtained from these fits are listed in Table 2. The values of the confinement radius, a_1, seem to be somewhat lower compared to our previous estimate of 6.5–10 Å, which was based on the low-Q behavior of the broader Lorentzian component. Besides, as one can see in Figure 8, even though eq 13 yields reasonable agreement with the data, there is a systematic deviation from the fit at higher Q. Thus, we have hypothesized that the localized diffusion process that we detected at 260 K, which was characterized by a characteristic confinement radius of 1.6 Å, might still contribute to the dynamics measured in the liquid phase. Therefore, we rewrote eq 13 to include a contribution from the localized process characterized
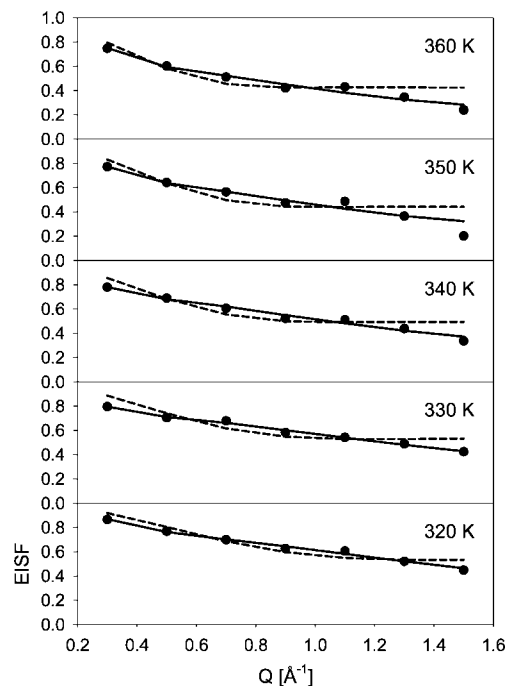
Figure 8. Spectral weight of the narrow Lorentzian component (parameter p obtained using eq 2 with $x = 0$ and eq 6 (symbols) fit with eq 13 (dashed lines) and eq 14 (solid lines).

TABLE 2: Parameters Obtained Using Fits of the Spectral Weight of the Narrow Lorentzian with Eqs 13 and 14[a]

	eq 13 fit		eq 14 fit			
T (K)	a_1 (Å)	c_1	a_1 (Å)	c_1	a_2 (Å)	c_2
360	4.9	0.42	7.3	0.67	1.6	0.37
350	4.4	0.44	7.6	0.72	1.6	0.4
340	4.2	0.49	8.6	0.75	1.5	0.42
330	3.9	0.53	8.7	0.77	1.3	0.42
320	3.2	0.53	6.5	0.80	1.2	0.4

[a] The c_2 values were free variables in the 330, 340, and 360 K data fits and were fixed at 0.40 for the 320 and 350 K data fits.

by an "immobile" fraction c_2 and a confinement radius a_2:

$$p(Q) = \left[c_1 + (1 - c_1)\left(\frac{3j_1(Qa_1)}{Qa_1}\right)^2\right][c_2 + (1 - c_2)j_0^2(Qa_2)] \quad (14)$$

For substantially different confinement radii, such that $a_1 \gg a_2$, eq 14 predicts two plateaus because $p(Q\rightarrow 0) = 1$, $p(1/a_1 \ll Q \ll 1/a_2) = c_1$, and $p(Q\rightarrow\infty) = c_1c_2$. As one can see in Figure 8, eq 14 yields much better fits compared to those obtained using eq 13. Besides, the fit values of the parameter a_1 listed in Table

2 are now in much better agreement with the previously estimated $a_1 = 6.5-10$ Å. In addition, the fit values of the parameter a_2 listed in Table 2 are reasonably close to the estimate of 1.6 Å obtained for the localized diffusion process evident in the 260 K data, suggesting that the spatial characteristics of this diffusion process may not change too much above the melting temperature.

It should be noted that some "rattling" of ions before escaping from a long-lived cage has been observed in a molecular dynamics simulation of 1-ethyl-3-methylimidazolium nitrate (EMIM-NO₃) ionic liquid.[12] Even though the in-cage "rattling" process on the time scale of tens of picoseconds was characterized by subdiffusive rather than diffusive behavior of the mean square displacements of the ions, the results of this simulation bear some resemblance to our observation of a spatially constrained, faster diffusion process in addition to the unrestricted diffusion process.

A spatially constrained diffusion process may be directly associated with the presence of clusters or other inhomogeneous regions in [H₂NC(dma)₂][BETI]. Clustering effects have been observed experimentally in imidazolium ionic liquids using fast atom bombardment mass spectrometry[28] and electron spray mass spectrometry.[29,30] Small structural clusters have been postulated to exist even in the gas phase, while in the solid and liquid phases these ionic liquids were described as nanostructured or nanoinhomogeneous materials.[30] Molecular dynamics simulation results[12] have suggested dynamically heterogeneous behavior in 1-ethyl-3-methylimidazolium nitrate (EMIM-NO₃), where more mobile ions form well-defined domains. These domains are not static; instead, the ions which are more mobile at a given time become less mobile at a later time.[12] The characteristic confinement radius of about 8 Å for the faster diffusion process measured in this work compares reasonably well with the characteristic size of the clusters comprised of mobile ions in the simulation.[12] Remarkably, at any given time only a fraction (some 8−9%) of the total number of ions in the simulation formed domains characterized by enhanced mobility.[12] This is consistent with our finding that the faster localized diffusion process involved only a fraction of protons in the [H₂NC(dma)₂][BETI] sample, whereas the larger fraction of protons (some 70−80%), described by the parameter c_1 in eqs 13 and 14, did not participate in this localized process. On the other hand, the slower unrestricted diffusion process describes the mobility of ions measured over longer periods of time and greater distances, where dynamic heterogeneities are averaged over, and the normal diffusive behavior is regained for all the ions in the sample.

We suggest that the identification of the faster localized diffusion process may provide indirect experimental evidence of spatial nonhomogeneity in [H₂NC(dma)₂][BETI] and, possibly, ionic liquids in general.

Diffusion Coefficients. We have attempted fitting the QENS data from the liquid phase using three Lorentzian components, but found it difficult because of the strong scatter in the fit parameters at most of the Q points, even though the agreement factors of the fits have improved, indicating probable presence of the third component. Most likely, the broadest component originating from the localized diffusion process with a confinement radius of 1.6 Å was difficult to resolve because of the relatively high background in the experiment. Therefore, we had to evaluate the diffusion coefficient of the localized diffusion process based on the lower-temperature data. We have previously concluded, based on the detailed analysis of the 260 K data, that this process yields Q-independent QENS broadening.
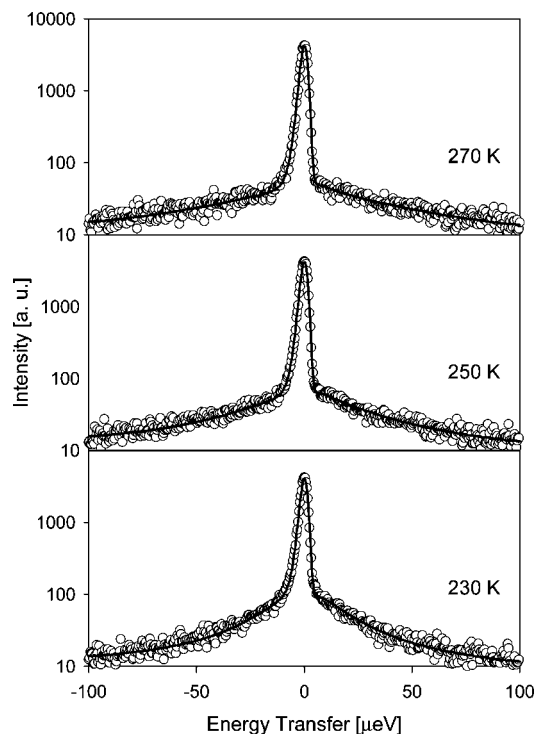

Figure 9. Fits obtained using eqs 2 and 3 (solid lines) of the Q-averaged data (symbols) collected while the temperature was ramped.

TABLE 3: Parameters Describing the Localized Diffusion Process Obtained Assuming a Confining Radius of 1.6 Å[a]

T (K)	$D \times 10^{-10}$ (m²/s)	$\tau \times 10^{-12}$ (s)
270	4.4 (0.6)	13.5 (0.9)
250	3.1 (0.4)	18.9 (0.8)
230	1.9 (0.2)	31.1 (0.8)

[a] Standard deviations are shown in parentheses.

Thus, we were able to analyze the 230, 250, and 270 K data sets obtained while the temperature was ramped by means of averaging over all Q values. This provided adequate statistic even for the data obtained in the course of the temperature ramp over the time period of a few minutes. The data and the fits obtained using eqs 2 and 3 are shown in Figure 9. The parameters describing the localized diffusion process are presented in Table 3. The local diffusion coefficients were obtained using a confining radius of 1.6 Å for the expression[26,27] that defines the hwhm of the QENS broadening as $\Gamma = 4.33D_{local}/a^2$.

Table 4 shows the diffusion parameters for the liquid phase obtained using eq 7. It should be noted that, according to eq 12, both the faster and slower translational diffusion components contribute to the hwhm of the broader Lorentzian. Furthermore, Figure 7 demonstrates that the widths of these two components are of the same order of magnitude. Therefore, we fit the difference between the values of Γ_1 and Γ_2 with eq 7, as shown in Figure 7c. The parameters obtained from the fits shown in Figure 7b,c are presented in Table 4. For comparison, translation diffusion coefficient of water is 22.99×10^{-10} m²/s and 35.75×10^{-10} m²/s at 298 and 318 K, respectively.[31]

Figure 10 summarizes the data for the diffusion coefficients. The activation energies obtained from Arrhenius fits are 447 ± 68 J/mol for the long-range, unrestricted translational diffusion in the liquid phase, 210 ± 58 J/mol for the spatially constrained translational diffusion process in the liquid phase, and 157 ± 8

TABLE 4: Diffusion Parameters in the Liquid Phase (Diffusion Coefficients, Characteristic Time between Jumps, and Mean Diffusion Jump Length) Obtained from the Fits Shown in Figure 7b,c that Characterize a Faster and a Slower Diffusion Process[a]

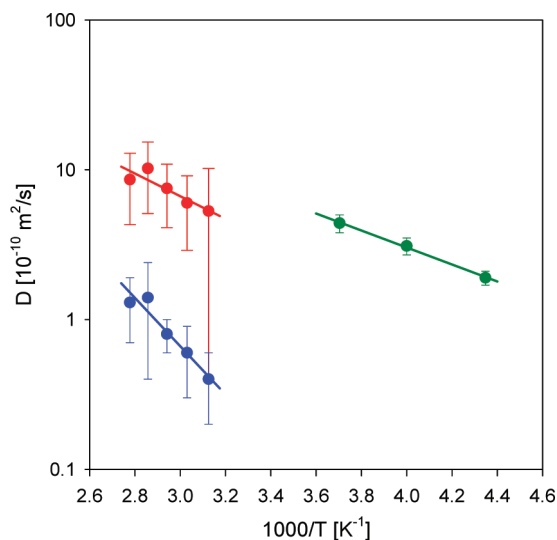|	faster diffusion process (fits in Figure 7c)			slower diffusion process (fits in Figure 7b)		
T (K)	$D \times 10^{-10}$ (m²/s)	$\tau \times 10^{-12}$ (s)	$(\langle L^2 \rangle)^{1/2} \times$ Å	$D \times 10^{-10}$ (m²/s)	$\tau \times 10^{-12}$ (s)	$(\langle L^2 \rangle)^{1/2} \times$ Å
360	8.6 (4.3)	18.2 (2.5)	3.1 (1.0)	1.3 (0.6)	42.1 (6.5)	1.8 (0.6)
350	10.2 (5.1)	24.8 (2.9)	3.9 (1.2)	1.4 (1.0)	82.2 (18.0)	2.6 (1.2)
340	7.5 (3.4)	23.0 (2.7)	3.2 (0.9)	0.8 (0.2)	64.8 (6.7)	1.8 (0.3)
330	6.0 (3.1)	24.7 (3.5)	3.0 (1.0)	0.6 (0.3)	66.0 (12.8)	1.5 (0.5)
320	5.3 (4.9)	25.0 (6.5)	2.8 (1.7)	0.4 (0.2)	92.2 (18.6)	1.5 (0.5)

[a] Standard deviations are shown in parentheses.

Figure 10. Temperature dependence of the diffusion coefficients describing a long-range translational diffusion process in the liquid phase (blue), a localized translational diffusion process in the liquid phase (red), and a localized process which is present in solid and liquid phases (green).

J/mol for the localized diffusion process that appears to be present in both liquid and solid phases. Based on extrapolating the data from the solid phase region into the liquid phase region, the localized diffusion process appears to be the fastest of three in the temperature range studied. It also has the lowest activation energy. The spatially constrained, faster of the two translational diffusion processes is characterized by the intermediate activation energy. Finally, the slowest, unrestricted long-range translational diffusion process exhibits the highest activation energy. It should be noted that, given a significant size of the errors bars shown in Figure 10, we cannot rule out a possibility that a non-Arrhenius (e.g., a VFT) temperature dependence of the translational diffusion coefficients could manifest itself in the data taken over a wider temperature range of the liquid phase.

Conclusion

In the studied temperature range of 30−360 K, we have found four distinct dynamic processes that contribute to the diffusion dynamics on the pico- to nanosecond time scale accessible in our QENS experiment. The first (and fastest) type of dynamics is attributed to rotations of the methyl groups. These dynamics are broadly distributed and become visible above approximately 100 K on the nanosecond time scale of our measurement. The second type of dynamics is attributed to a localized process with a characteristic confinement radius of about 1.6 Å, which most likely involves protons of the −NH₂ groups. Even though these

motions may take place at even lower temperatures, they become visible in our experiment above 240 K, following the crystallization transition, when the methyl group dynamics may become suppressed. In the amorphous phase below 240 K, the large number of protons in the methyl groups compared to those in the −NH₂ groups yields a scattering signal that is dominated by the former type of protons. The aforementioned two processes take place in both solid and liquid phases, even though the methyl group rotations above the melting temperature are likely to be far too fast to be detected in our experiment.

Above the melting temperature of about 290 K, we have found two new diffusion processes contributing to the dynamics of the liquid phase. Both of these processes appear to be of translational character. However, only the slower of them represents unrestricted translation diffusion. The faster process is better described as confined translational diffusion with a characteristic confinement radius of about 8 Å. The even faster localized process attributed to the dynamics of protons of the −NH₂ groups, which we observed in the crystalline phase between 240 and 290 K, could not be directly resolved in the QENS signal obtained from the liquid phase, but manifested itself in the relative spectral weights of the Lorentzian components. Among the three diffusion processes detected in the liquid phase, the lowest activation energy was associated with the fastest localized process, whereas the highest activation energy was exhibited by the slowest, long-range translational diffusion process. The spatially restricted translational diffusion was characterized by the intermediate activation energy. Therefore, the activation energy of various diffusion processes shows inverse dependence on the extent of spatial localization of the processes; lower activation energies are associated with more localized processes.

The properties of ultimate interest to the fuel cell application are related to the long-range proton diffusion parameters. Therefore, it seems likely that, despite the presence of faster, but spatially constrained processes, the long-range proton transfer in [H₂NC(dma)₂][BETI] may be associated primarily with the unrestricted translational diffusion process. This process is characterized by a diffusion coefficient varying from 0.4 × 10⁻¹⁰ to 1.4 × 10⁻¹⁰ m²/s in the temperature range of 320−360 K. The fact that there are two distinct translational diffusion processes on the time scale of tens of picoseconds in the liquid phase of [H₂NC(dma)₂][BETI] is probably the most important result of this work. The *Q*-resolution capabilities of QENS are essential for differentiating the unrestricted translational diffusion from other types of diffusion motions in [H₂NC-(dma)₂][BETI].

References and Notes

(1) Yoshizawa, M.; Xu, W.; Angell, C. A. *J. Am. Chem. Soc.* **2003**, *125*, 15411.

(2) Xu, W.; Angell, C. A. *Science* **2003**, *302*, 422.

(3) Noda, A.; Watanabe, M. *Electrochim. Acta* **2000**, *45*, 1265.

(4) Susan, M. A. B. H.; Noda, A.; Mitsushima, S.; Watanabe, M. *Chem. Commun.* **2003**, 938.

(5) Greaves, T. L.; Drummond, C. J *Chem. Rev* **2008**, *108*, 206. Greaves, T. L.; Drummond, C. J. *Chem. Rev* **2008**, *108*, 206.

(6) Maginn, E. J. *Acc. Chem. Res.* **2007**, *40*, 1200.

(7) Huang, J. F.; Luo, H. M.; Liang, C. D.; Sun, I. W.; Baker, G. A.; Dai, S. *J. Am. Chem. Soc.* **2005**, *127*, 12784.

(8) Huang, J. F.; Baker, G. A.; Luo, H. M.; Hong, K. L.; Li, Q. F.; Bjerrum, N. J.; Dai, S. *Green Chem.* **2006**, *8*, 599.

(9) Luo, H. M.; Baker, G. A.; Lee, J. S.; Pagni, R. M.; Dai, S., to be submitted for publication.

(10) Kolomeitsev, A. A.; Koppel, I. A.; Rodima, T.; Barten, J.; Lork, E.; Roschenthaler, G. V.; Kaljurand, I.; Kutt, A.; Koppel, I.; Maemets, V.; Leito, I. *J. Am. Chem. Soc.* **2005**, *127*, 17656.

(11) Kreuer, K. D.; Rabenau, A.; Weppner, W. *Angew. Chem., Int. Ed. Engl.* **1982**, *21*, 208.

(12) Del Pópolo, M. G.; Voth, G. A. *J. Phys. Chem. B* **2004**, *108*, 1744.

(13) Del Pópolo, M. G.; Lynden-Bell, R. M.; Kohanoff, J. *J. Phys. Chem. B* **2005**, *109*, 5895.

(14) Triolo, A.; Russina, O.; Arrighi, V.; Juranyi, F.; Janssen, S.; Gordon, C. M. *J. Chem. Phys.* **2003**, *119*, 8549.

(15) Triolo, A.; Russina, O.; Hardacre, C.; Nieuwenhuyzen, M.; Gonzalez, M. A.; Grimm, H. *J. Phys. Chem. B* **2005**, *109*, 22061.

(16) Triolo, A.; Mandanici, A.; Russina, O.; Rodriguez-Mora, V.; Cutroni, M.; Hardacre, C.; Nieuwenhuyzen, M.; Bleif, H.-J.; Keller, L.; Ramos, M. A. *J. Phys. Chem. B* **2006**, *110*, 21357.

(17) Inamura, Y.; Yamamuro, O.; Hayashi, S.; Hamaguchi, H. *Physica B* **2006**, *385−386*, 732.

(18) Herwig, K. W.; Keener, W. S. *Appl. Phys. A: Mater. Sci. Process.* **2002**, *74*, S1592.

(19) Mamontov, E.; Zamponi, M.; Hammons, S.; Keener, W. S.; Hagen, M.; Herwig, K. W. *Neutron News* **2008**, *19*, 22.

(20) https://neutronsr.us/portal//.

(21) Frick, B.; Fetters, L. J. *Macromolecules* **1994**, *27*, 974.

(22) Roh, J. H.; Novikov, V. N.; Gregory, R. B.; Curtis, J. E.; Chowdhuri, Z.; Sokolov, A. P. *Phys. Rev. Lett.* **2005**, *95*, 038101.

(23) Bée, M. *Quasielastic Neutron Scattering*; Hilger: Bristol, UK, 1988.

(24) Singwi, K. S.; Sjölander, A. *Phys. Rev.* **1960**, *119*, 863.

(25) Egelstaff, P. A. *An Introduction to the Liquid State*; Academic Press: London, 1967.

(26) Volino, F.; Dianoux, A.-J. *Mol. Phys.* **1980**, *41*, 271.

(27) Bellissent-Funel, M.-C.; Chen, S. H.; Zanotti, J.-M. *Phys. Rev. E.* **1995**, *51*, 4558.

(28) AbdulSada, A. K.; Elaiwi, A. E.; Greenway, A. M.; Seddon, K. R. *Eur. Mass Spectrosc.* **1997**, *3*, 245.

(29) Gozzo, F. C.; Santos, L. S.; Augusti, R; Consorti, C. S.; Dupont, J.; Eberlin, M. N. *Chem. Eur. J.* **2004**, *10*, 6187.

(30) Dupont, J. *J. Braz. Chem. Soc.* **2004**, *15*, 341.

(31) Mills, R. *J. Phys. Chem.* **1973**, *77*, 685.